technologies

MDPI

*Article*

# Design and Development of an Electronic Interface for Acquiring Signals from a Piezoelectric Sensor for Ultrasound Imaging Applications

**Elizabeth Espitia-Romero [1], Adriana Guzmán-López [2], Micael Gerardo Bravo-Sánchez [2,*], Juan José Martínez-Nolasco [3], José Alfredo Padilla Medina [4] and Francisco Villaseñor-Ortega [2]**

[1] Departamento de Posgrado e Investigación (DEPI), Tecnológico Nacional de Mexico (TecNM), Instituto Tecnológico de Celaya (ITC), Celaya 38010, Guanajuato, Mexico; elizabeth.espitia@itcelaya.edu.mx
[2] Departamento de Ingeniería Bioquímica e Ingeniería Ambiental, Tecnológico Nacional de Mexico (TecNM), Instituto Tecnológico de Celaya (ITC), Celaya 38010, Guanajuato, Mexico; adriana.guzman@itcelaya.edu.mx (A.G.-L.); francisco.villasenor@itcelaya.edu.mx (F.V.-O.)
[3] Departamento de Ingeniería Mecatrónica, Tecnológico Nacional de Mexico (TecNM), Instituto Tecnológico de Celaya (ITC), Celaya 38010, Guanajuato, Mexico; juan.martinez@itcelaya.edu.mx
[4] Departamento de Ingeniería Electrónica, Tecnológico Nacional de Mexico (TecNM), Instituto Tecnológico de Celaya (ITC), Celaya 38010, Guanajuato, Mexico; alfredo.padilla@itcelaya.edu.mx
* Correspondence: gerardo.bravo@itcelaya.edu.mx

**Abstract**

The increasing demand for accurate and accessible medical imaging has driven efforts to develop technologies that overcome limitations associated with conventional imaging techniques, such as MRI and CT scans. This study presents the design and implementation of an electronic interface for acquiring signals from a piezoelectric ultrasound sensor with the aim of improving image reconstruction quality by addressing electromagnetic interference and speckle noise, two major factors that degrade image fidelity. The proposed interface is installed between the ultrasound transducer and acquisition system, allowing real-time signal capture without altering the medical equipment's operation. Using a printed circuit board with 110-pin connectors, signals from individual piezoelectric elements were analyzed using an oscilloscope. Results show that noise amplitudes occasionally exceed those of the acoustic echoes, potentially compromising image quality. By enabling direct observation of these signals, the interface facilitates the future development of analog filtering solutions to mitigate high-frequency noise before digital processing. This approach reduces reliance on computationally expensive digital filtering, offering a low-cost, real-time alternative. The findings underscore the potential of the interface to enhance diagnostic accuracy and support further innovation in medical imaging technologies.

**Keywords:** ultrasound; interface; piezoelectric sensor; analog filter; image reconstruction

check for updates

Academic Editor: Valeri Mladenov

Received: 3 May 2025
Revised: 13 June 2025
Accepted: 15 June 2025
Published: 25 June 2025

**Citation:** Espitia-Romero, E.; Guzmán-López, A.; Bravo-Sánchez, M.G.; Martínez-Nolasco, J.J.; Padilla Medina, J.A.; Villaseñor-Ortega, F. Design and Development of an Electronic Interface for Acquiring Signals from a Piezoelectric Sensor for Ultrasound Imaging Applications. *Technologies* **2025**, *13*, 270. https://doi.org/10.3390/technologies13070270

**Copyright:** © 2025 by the authors. Licensee MDPI, Basel, Switzerland. This article is an open access article distributed under the terms and conditions of the Creative Commons Attribution (CC BY) license (https://creativecommons.org/licenses/by/4.0/).

## 1. Introduction

The generation of diagnostic images is a highly significant area of research in biomedicine. Currently, medical imaging plays a crucial role in the rapid diagnosis and monitoring of the progression of various diseases. Some of its most relevant applications include cancer detection, monitoring of changes in cancerous tissues, muscle injuries, evaluation of blood vessels, joint analysis, internal organ observation, fetal examination during pregnancy, kidney stone monitoring, physiotherapy assessment, and analysis of cosmetic

surgeries [1–3]. Magnetic resonance imaging (MRI) [4], positron emission tomography (PET) [5], computed tomography (CT) [6,7], laser scanning confocal microscopy (LSCM) [8], photoacoustic imaging (PA) [9,10], and hybrid techniques such as MRI-PA, which demonstrated excellent performance [11], are among the technologies that rely primarily on image interpretation. However, these methods are often limited by the need for exogenous contrast agents, exposure to radiation, and high costs. Developing reliable and accessible technologies to support medical diagnosis remains a constant challenge. Ultrasound imaging presents an attractive alternative, enabling faster and more accurate diagnoses. It does not require contrast agents and operates based on the principles of acoustic wave propagation through piezoelectric elements, electronics, and clinical research, to reconstruct images from ultrasonic signals [12,13]. These systems offer significant advantages: they utilize non-ionizing energy, are non-invasive, provide real-time data, and can represent images of both structural or anatomical dimensions (mm) and functional scales (μm) [14,15].

The study of acoustic waves is a research area of high interest. Currently, the literature presents various proposals based on physical principles that involve the generation of acoustic waves using pulsed laser light, such as for monitoring the elimination of nanoparticles in the kidneys of a live mouse [16]; detection and imaging of defects in metallic components [17]; image reconstruction of breast tissue for the detection of malignant lesions [18]; deep learning algorithms aimed at improving medical diagnoses through imaging using ultraviolet light in photoacoustic applications on thin human tissue samples [19]; and automatic classification of breast tumors in ultrasound imaging, showing improved diagnostic accuracy [20]. Additional applications include the detection of high-temperature points for fire prevention and control [21], classification of dehydrated strawberries and fruit ripeness using artificial neural networks [22], studies on human cadaver heads to identify optimal acoustic receiver locations for minimally invasive, image-guided neurosurgery [23], and acoustic waves applied to biodetection tasks such as cell manipulation and the quantification of proteins, vapor molecules, and DNA hybridizations [24,25]. Acoustic wave techniques have also been applied in the food industry, particularly in the development of food processing methods for cell destruction and intracellular material extraction. Ultrasonic processes can activate microorganisms and enzymes to preserve or decontaminate food, especially when ultrasound is combined with heat and high-pressure techniques [26]. Proposals aimed at improving the tangential resolution of systems with a finite number of sensors include multi-angle systems that rotate around the sample to subsequently generate the image [27]. Other studies highlight the importance of enhancing image reconstruction algorithms, such as SPANNER, which addresses artifact reduction through precise modeling [28], or the lag-based delay multiply and sum combined with coherence factor (DMAS-LAG-CF) algorithm, which improves resolution and contrast for distinguishing malignant from benign ovarian lesions [29]. Another technique, the single sensor scan synthetic aperture focusing technique (SSC-SAFT), demonstrates the ability to eliminate sidelobe artifacts and comet tail artifacts [30]. A realistic ultrasound image simulation tool developed in MATLAB for educational and research purposes has also been introduced, named the Matlab UltraSound Toolbox (MUST) [31].

Similarly, other studies mention the two main categories of artifacts in acoustic imaging: those related to assumptions made by the ultrasound imaging system, and those caused by interference within the equipment. These artifacts can lead to incorrect diagnoses, as they obscure and degrade the quality of the resulting image [32,33]. To mitigate axial artifacts—typically located beneath the actual image and consisting of acoustic reverberations that prolong the wave travel time—image reconstruction algorithms have been implemented. One proposed approach involves signal restoration prior to applying conventional methods such as delay and sum (DAS) and delay multiply and sum

(DMAS), demonstrating a 45% improvement in image resolution and contrast, and an 80% suppression of background artifacts [34]. Regarding artifacts caused by electromagnetic interference in the equipment, these are attributed to factors such as insufficient shielding, transducer operation issues, inadequate sampling frequency—which may induce aliasing artifacts—and the limited processing speed of image reconstruction algorithms. These types of interference result in speckle noise in ultrasound images, which degrades the visual quality and impairs accurate human interpretation by introducing a grainy pattern [35,36]. In [37], a comparative study was conducted on noise reduction methods to improve the ultrasound image reconstruction of blood cells. The study examined low-pass, band-pass, and discrete wavelet transform (DWT)-based filters implemented using MATLAB's Signal Processing Toolbox and Wavelet Toolbox functions. Evaluation metrics such as root mean square error (RMSE), signal-to-noise ratio (SNR), and contrast-to-noise ratio (CNR) were used to assess performance.

Additionally, ref. [38] presents a speckle noise removal proposal through a filtering algorithm applied directly to medical images, employing speckle reducing anisotropic diffusion (SRAD), discrete wavelet transform (DWT) using symmetry characteristics, weighted guided image filtering (WGIF), and gradient domain guided image filtering (GDGIF). The results show effective speckle noise suppression while preserving the edge information of the imaged objects. Finally, ref. [39] explores a study of twenty-seven techniques aimed at smoothing or eliminating speckle noise in ultrasound images. This study compared spatial filtering, diffusion filtering, wavelet filtering, and machine learning techniques focused on deep learning. Although classical and hybrid filtering methods provided accurate results in reducing noise and preserving information, they typically required manual parameter tuning, as their effectiveness depends heavily on the nature of the input data. On the other hand, machine learning techniques face limitations due to the difficulty of acquiring clean and representative training data, particularly in real-world clinical scenarios. With the objective of addressing speckle noise reduction and the associated challenges in enhancing the quality of diagnostic ultrasound imaging, this work proposes the use of a piezoelectric sensor coupled to medical equipment through a custom-designed electronic interface for the acquisition of acoustic signals. This strategy aims to provide innovative solutions in a more efficient and timely manner. The main contributions of this article are summarized as follows:

- The design and development of an electronic interface for acquiring ultrasonic signals generated by a piezoelectric transducer in a commercial ultrasound device, with a focus on improving medical image reconstruction.
- The implementation of a low-cost, modular, and replicable acquisition system that can be integrated into future portable medical imaging solutions.
- The functional validation through the acquisition of real signals and testing under controlled experimental conditions, providing preliminary evidence of its potential usefulness for future clinical and research applications.

As a novel aspect, this study analyzes the underlying causes of speckle noise in medical images and reviews previous research that proposes alternatives based on sensor design and image reconstruction algorithms. In such studies, the acquisition process is often time-consuming due to the use of a single sensor per test. In contrast, this work presents an accessible, functional, and efficient solution.

The article is organized as follows: Section 2 describes the design and technical specifications of the electronic interface, as well as the development of the biological tissue emulator and the experimental methods employed. Section 3 presents the obtained results, which are discussed in Section 4. Finally, Section 5 outlines the conclusions and projections for future work.

## 2. Electronic Interface Design

Ultrasound waves are produced by transducers activated at frequencies above 20 kHz, which is commonly accepted as the upper frequency limit of human hearing. Figure 1 shows a typical ultrasound hardware system, which mainly consists of a transducer, an ultrasonic pulse transmitter, a receiver, a logic control unit, a storage system, and a display unit [40].

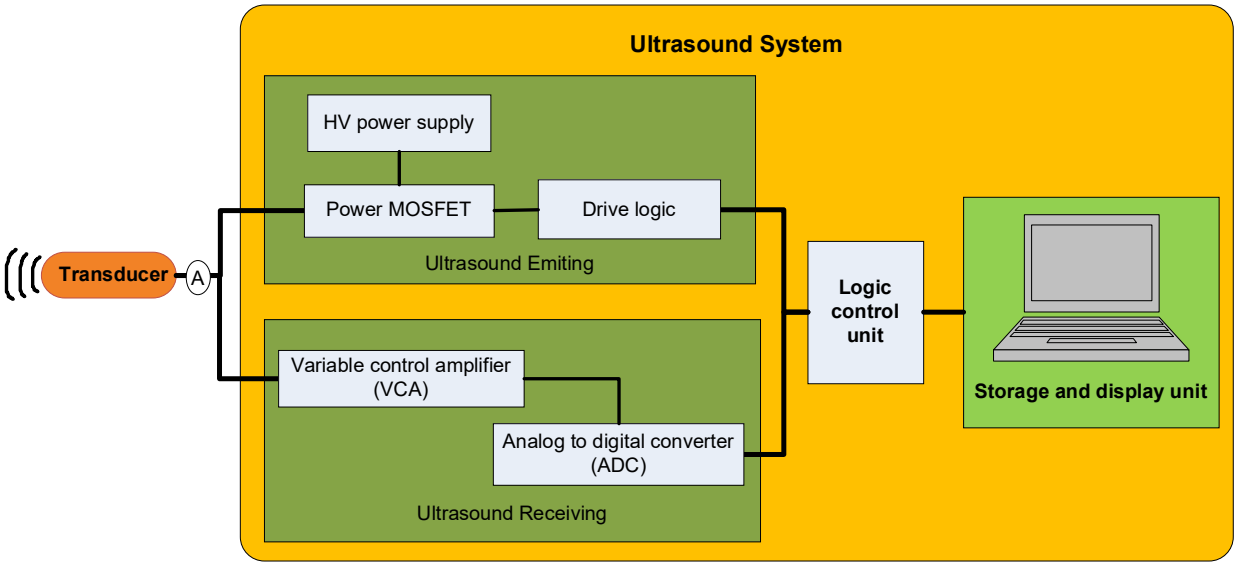



**Figure 1.** Diagram of the typical hardware system of ultrasound equipment.

The ultrasonic pulse transmitter comprises high-power MOSFETs, a logic controller, and a high-voltage power supply. The receiver is primarily composed of a voltage-controlled amplifier (VCA) and an analog-to-digital converter. In our case, this system operates correctly and has been validated for medical applications in small animal species. However, the images generated still contain noise, complicating diagnosis due to difficulties in interpreting the images. Therefore, the electronic interface developed in this work aims to visualize signals directly from the transducer in real time, without any processing. The interface is placed immediately after the connection port between the transducer and the signal acquisition board within the ultrasound system's medical equipment. This connection point is indicated by the letter 'A' in Figure 1.

At point A in Figure 1, there is a convex-type transducer with 80 ceramic elements, known as piezoelectric materials, which convert acoustic energy into electrical signals and vice versa. When a voltage is applied to the piezoelectric element, the material undergoes expansion and/or contraction, thereby generating an acoustic signal [41,42]. The transducer at point A is connected to the medical ultrasound equipment, where the emission and reception of acoustic signals take place. The schematic shown in Figure 2 illustrates how the proposed electronic interface is connected, with the purpose of observing the experimental signals in real time without interfering with the operation of the medical device. As shown, the medical ultrasound system (a) is directly connected to the proposed electronic interface (b). This printed circuit board (PCB) is designed to connect in parallel with both the transducer (c) and the signal acquisition system or oscilloscope (d). The oscilloscope enables the acquired signals to be processed via a computer, allowing for the reconstruction of an alternative ultrasound image.

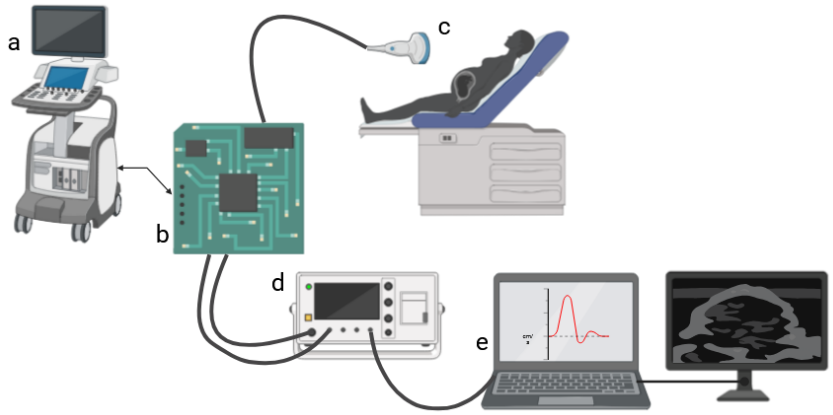



**Figure 2.** The proposed interconnection is shown; (**a**) medical ultrasound equipment, (**b**) proposed electronic interface, (**c**) transducer, (**d**) oscilloscope, and (**e**) computer/monitor.

Initially, an inspection is conducted to understand the electronic configuration connecting the transducer to the ultrasound system. The transducer connection port on the equipment contains 110 pins which transmit electrical signals between components. For the design of the proposed electronic interface, it is essential to determine the pin configuration and the type of signals each pin carries. The design process began with the development of the printed circuit board (PCB) that constitutes the proposed electronic interface. This PCB features three 110-pin connectors and 220 laminated conductive tracks that provide interconnection between the ports. Figures 3 and 4 display the six layout layers, each showing the routing of approximately 36 tracks per layer for port interconnection. The tracks are evenly distributed, which is critical to ensure optimal performance and to avoid any signal distortion or interference with the medical ultrasound system due to electromagnetic incompatibility between components [43,44]. Table 1 presents the technical and manufacturing specifications of the PCB.

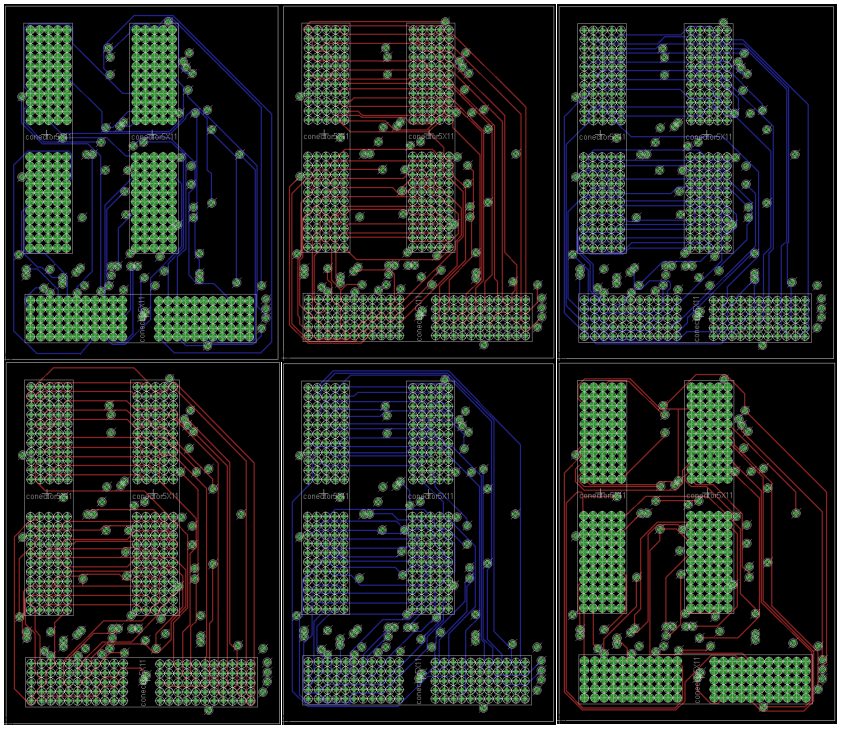
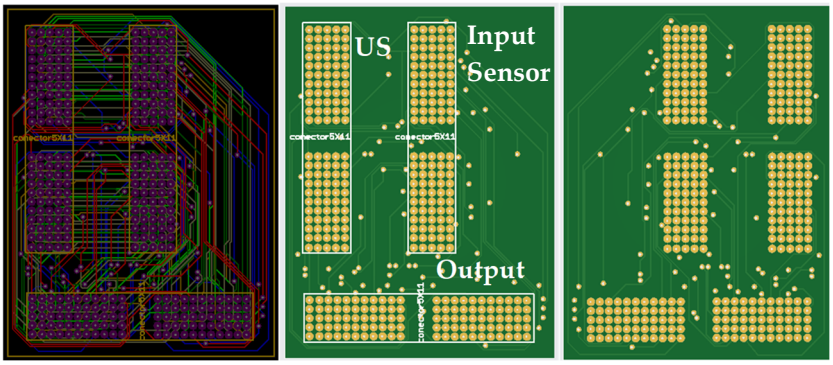


**Figure 3.** Interface board plans.




(**a**) (**b**) (**c**)

**Figure 4.** 2D view of (**a**) six planes with the 220 tracks, (**b**) top PCB, and (**c**) bottom PCB of the proposed electronic interface.

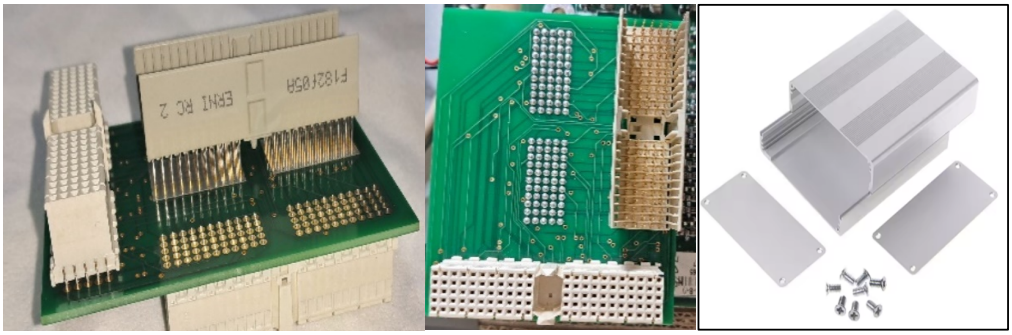
**Table 1.** Electronic interface design data.

| Parameter | Specification |
|---|---|
| Phenolic board material | Epoxy fiberglass |
| Maximum deformation temperature | 130 °C |
| Breakdown voltage | 3000 V |
| Thermal conductivity | 1 W/mK |
| Copper weight | 1 OZ |
| Color | Verde |
| Phenolic board dimensions | 60 mm × 78 mm |
| Number of planes | 6 planes |
| Plate thickness | 1.6 mm |
| Average number of tracks per plan | 36 |
| Inlet and outlet port dimensions | 10 mm × 50 mm |

Subsequently, the installation of the terminals for the three CompactPCI (CPCI) ports—two female and one male, each with 110 pins—is carried out on the fabricated printed circuit board using commercially available solder composed of 60% tin and 40% lead. Figure 5 shows the PCB with the port terminals installed. Finally, the proposed electronic interface board is connected to the medical ultrasound system at the terminal that contains the transducer connection port. The interface includes a housing made of anodized aluminum alloy, which is grounded as part of the electromagnetic shielding. This enclosure contains the interface, which is properly insulated, and uses aluminum screws with washers to maintain electrical conductivity. These screws are used to connect both the interface and the equipment to the chassis ground terminal. The enclosure has a thickness of 4 mm, which enhances low-frequency attenuation, and features a type II anodized finish, improving its resistance to corrosion.

The acquisition of signals through the electronic interface connected simultaneously to the ultrasound equipment and the transducer allows for the observation and parallel acquisition of signals emitted and received by each of the piezoelectric elements in the transducer. To perform this process effectively, a stable environment is required to ensure proper intervention, including the preparation of a biological tissue emulator and the selection of an observation object. As the observation object, a 50-cent Mexican coin was selected. Its physical characteristics are shown in Figure 6. This coin has a diameter of 17 mm, a thickness of 1.9 mm, and a weight of 3.103 g. It features a reeded edge and is made of stainless steel. The composition of this stainless steel includes 16% chromium, 0.75%

nickel, 0.12% carbon, 1% silicon, 1% manganese, 0.03% sulfur, and 0.04% phosphorus, with the remaining percentage being iron [45].



(**a**) (**b**) (**c**)

**Figure 5.** Proposed electronic interface (**a**) prior to soldering and (**b**) with all three ports soldered (**c**) made of anodized aluminum.

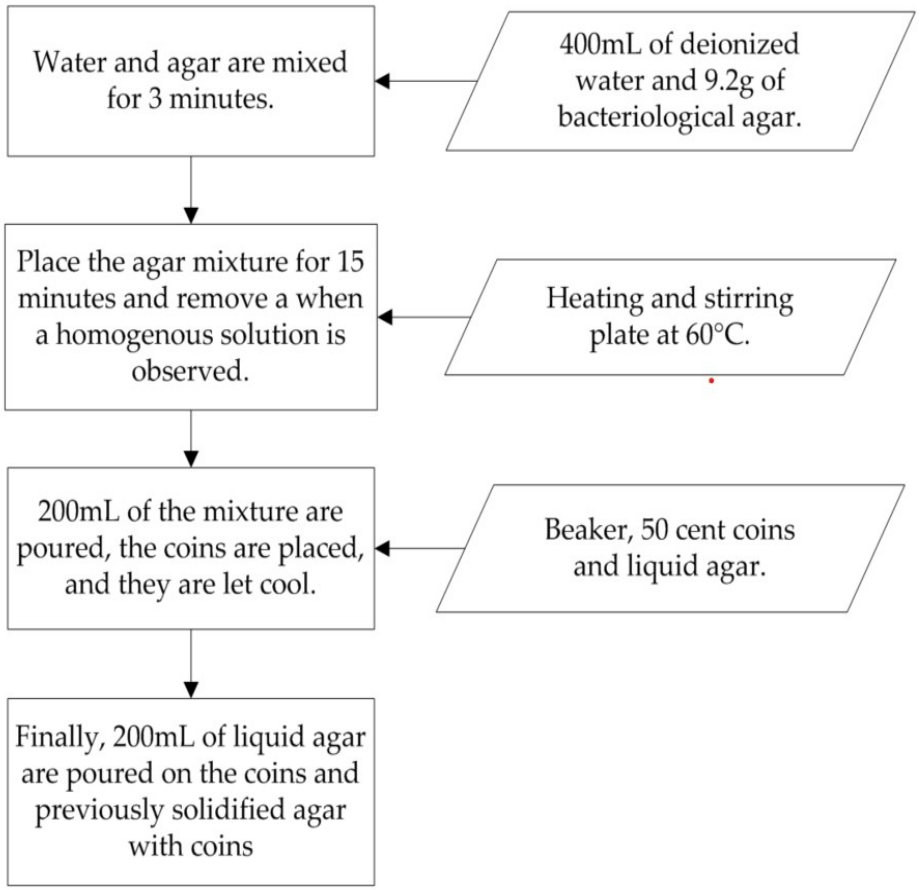



**Figure 6.** Process diagram for the development of a biological tissue emulator.

To prepare a 400 mL biological tissue emulator gel, bacteriological agar is used. This type of agar is widely employed as a tissue-mimicking material due to its notable properties, including gelation at room temperature between 32 °C and 38 °C, with a gel strength of 750 g/cm$^2$ which provides suitable firmness, chemical inertness, uniform distribution in gelled media, and ease of preparation [10].

Figure 6 presents a diagram of the preparation method for 400 mL of agar-based gel. The procedure requires 400 mL of deionized water and powdered agar. Initially, 400 mL

of deionized water and 9.2 g of agar are poured into a beaker. The water and agar are then mixed for approximately 3 min, after which the mixture is placed on a heating and stirring plate at 60 °C for 15 min, or until a homogeneous solution is observed. From the homogeneous mixture, 200 mL are poured into a separate beaker and allowed to cool for 5 min at room temperature (25 °C). Five coins are then positioned vertically in the solidified agar. The remaining liquid agar is poured over the beaker containing the embedded coins and left to cool for 5 min at room temperature, or alternatively, the beaker can be covered and refrigerated. Finally, the transducer of the ultrasound system is mounted on a universal stand above the prepared tissue emulator and adjusted until the coin images become visible on the ultrasound display.

## 3. Results

To evaluate the acquired signals, measurements were carried out using an oscilloscope connected to the port of the electronic interface positioned between the ultrasound system and the transducer. The oscilloscope used was a UNI-T UPO1202CS model, featuring a sampling rate of 1 GS/s. Among the 110 pins monitored on the electronic interface, 80 were identified as ultrasonic signal lines corresponding to each piezoelectric element in the transducer connected to the system. Additionally, 26 pins were identified as ground reference signals (GND), 2 pins carried 5 V DC signals, and 2 pins carried 3 V DC signals. Figure 7 illustrates the pin configuration of the electronic interface port, with each signal numbered consecutively to indicate its correspondence to the individual transducer elements (a) that comprise the ultrasound sensor (b) within the system.

| | | | | | | | | | | | | | | | | | | | | |
|---|---|---|---|---|---|---|---|---|---|---|---|---|---|---|---|---|---|---|---|---|
| 5V | 5V | 1 | 3 | 6 | 11 | GND | 19 | 23 | 28 | 32 | | GND | 40 | 44 | 48 | 52 | GND | 61 | 65 | 69 | 73 | GND |
| GND | GND | 2 | 4 | 7 | GND | 15 | 20 | 24 | 29 | 33 | | 37 | 41 | GND | 49 | 53 | 57 | 62 | 66 | 70 | GND | 77 |
| GND | 3V | GND | GND | 8 | 12 | 16 | 21 | 25 | GND | 34 | | 38 | 42 | 45 | GND | 54 | 58 | 63 | 67 | GND | 74 | 78 |
| GND | GND | GND | GND | 9 | 13 | 17 | 22 | 26 | 30 | 35 | | GND | 43 | 46 | 50 | 55 | 59 | 64 | GND | 71 | 75 | 79 |
| 3V | GND | GND | 5 | 10 | 14 | 18 | GND | 27 | 31 | 36 | | 39 | GND | 47 | 51 | 56 | 60 | GND | 68 | 72 | 76 | 80 |

(**a**)




(**b**)

**Figure 7.** Schematic of (**a**) distribution of the 110 signals at the interface port and (**b**) transducer with the distribution of the 80 piezoelectric elements.

Figure 7a shows the port that constitutes the electronic interface, in which the numbers corresponding to the piezoelectric transducers forming the sensor head are highlighted in green, the ground reference signals (GND) in yellow, and the DC voltage lines (5 V and 3 V) in white. The sensor head, depicted in Figure 7b, contains 80 piezoelectric elements arranged consecutively within the head, specifically in the insulating window that makes contact with the biological tissue emulator. These elements in Figure 7b correspond directly to the numbering indicated on the electronic interface in Figure 7a. Following the mapping of the piezoelectric elements and the electronic interface, all 110 signals were acquired from the interface in real time, operating in parallel with the ultrasound system (including 80 ultrasound transmit–receive signals, 26 ground reference signals, and 4 direct current voltage lines). From the 80 ultrasonic signals, a representative subset of 30 signals was selected for image representation. These selected signals are displayed in Figures 8–10. The sensor ranges shown in these figures correspond to piezoelectric transducers numbered 1–10, 31–40, and 71–80, respectively.

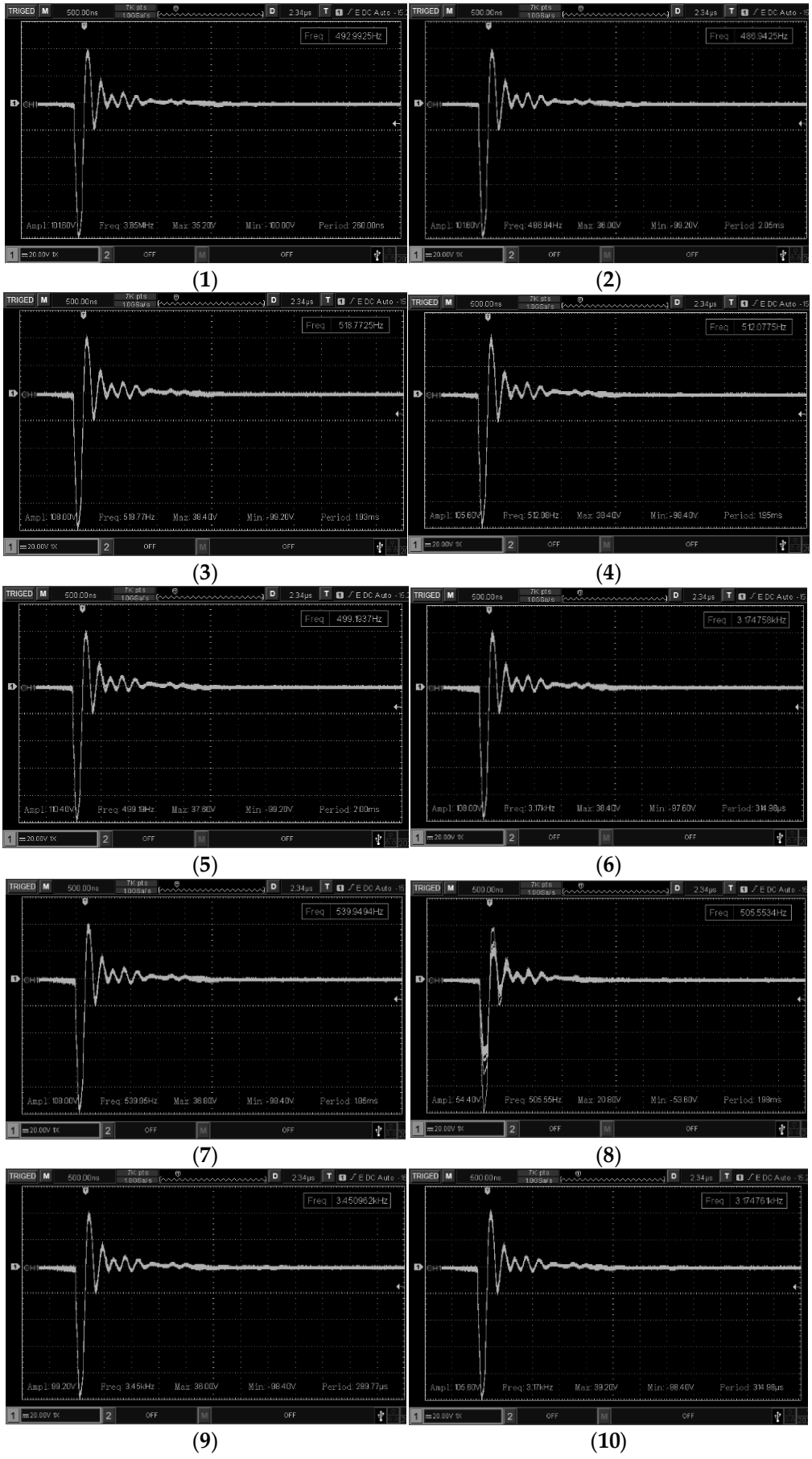



**Figure 8.** Acoustic signals from the piezoelectric sensor **1–10**.

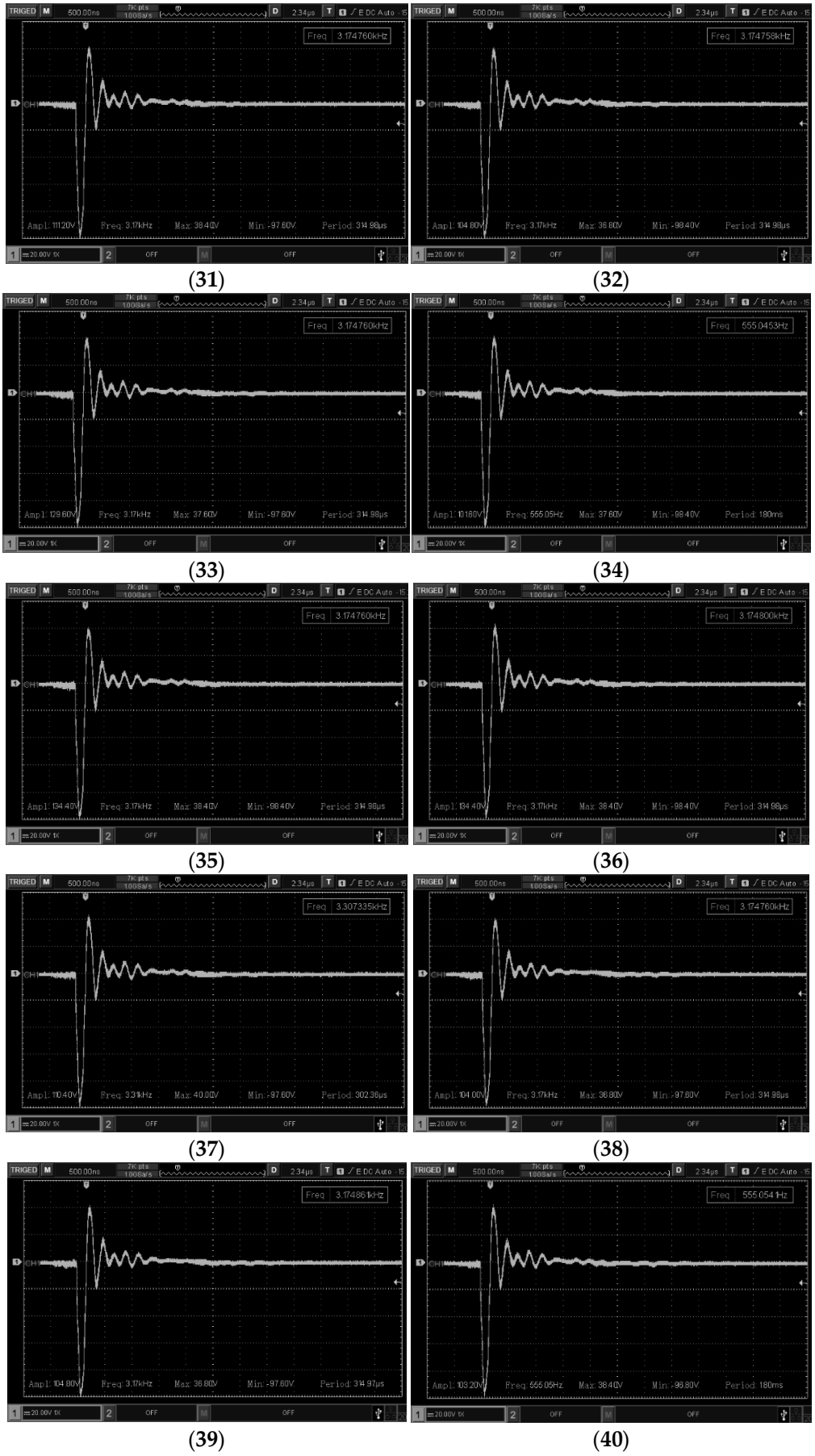



**Figure 9.** Acoustic signals from the piezoelectric sensor **31**–**40**.

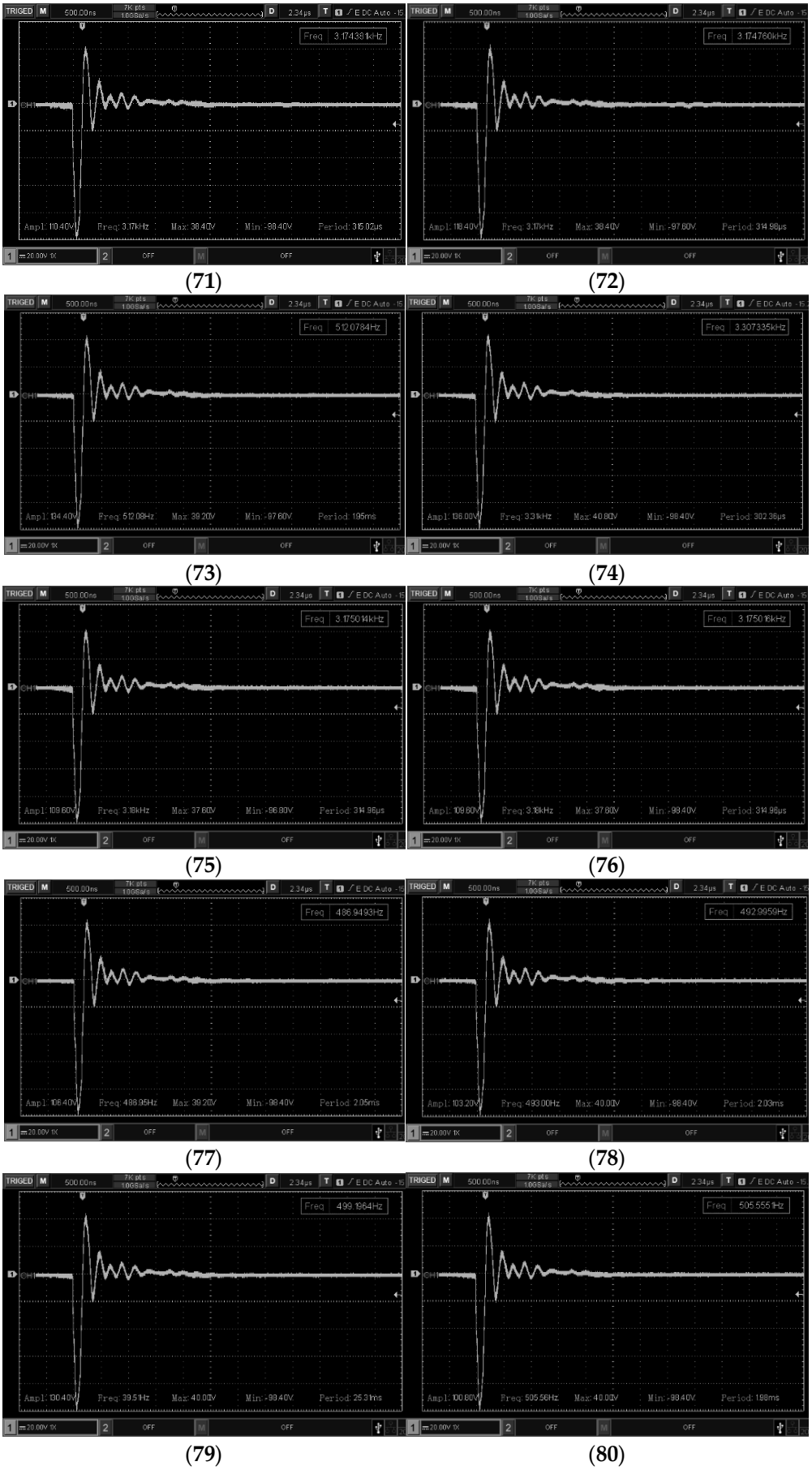



**Figure 10.** Acoustic signals from the piezoelectric sensor **71**–**80**.

Figure 8 shows the acquired signals corresponding to piezoelectric transducers numbered 1 through 10. These signals clearly exhibit both the transmission and the reception of the ultrasound echo. The measurements were obtained using a conventional probe with no attenuation adjustment, set at 20 volts/div. The transmission pulses reached amplitudes of up to 150 volts, while the echo signals displayed varying amplitudes at a frequency of 3.5 MHz. The amplitude of the echo signals ranged from approximately 200 mV to 1.84 V.

Figure 9 displays the acquired signals from piezoelectric transducers numbered 31 through 40. These signals show both the transmission and reception of ultrasound echoes. The measurements were taken using a conventional probe without attenuation adjustment, set at 20 volts/div. The transmitted signals reached amplitudes of up to 150 volts, while the echoes exhibited varying amplitudes at a frequency of 3.5 MHz. The amplitude of the echo signals ranged from approximately 400 mV to 1.6 V.

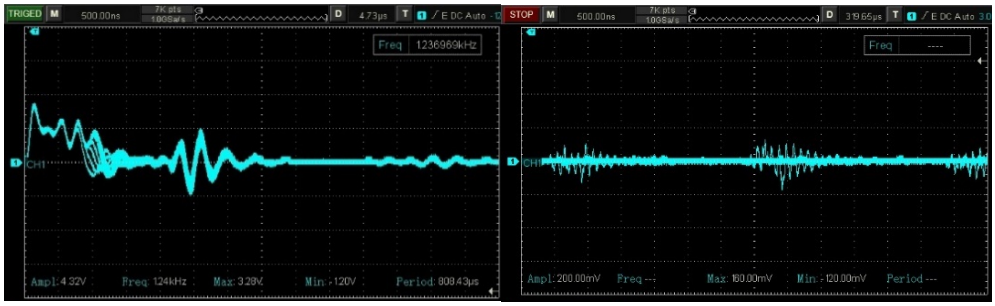
Likewise, Figure 9 shows the acquired signals corresponding to the piezoelectric transducers numbered 71 to 80, in which the emission and reception of the ultrasound signal echo can be observed. These signals (Figures 8–10) were obtained using a conventional probe without attenuation adjustment. Figure 11 presents a zoomed-in view at the focal distance of the image obtained by the oscilloscope for the acoustic signal. The central frequency of 3.046 MHz is indicated on the screen. This corresponds to the fundamental frequency of the acoustic signal detected by the sensor. Voltage scale: the signal is shown on a scale of 20.0 V per vertical division (CH1). Time scale: the horizontal scale is 400 nanoseconds (ns) per division, with a sampling rate of 500 MS/s (millions of samples per second). Waveform: Presents a main pulse with a very pronounced positive peak, followed by a larger negative peak, and produces a series of damped oscillations. This is characteristic of an acoustic echo signal, where the initial pulse represents the arrival of the main wave and the subsequent oscillations can correspond to reverberations or internal echoes. To clearly observe the amplitude of the echoes. Figure 12 presents a zoomed-in view at the focal distance of the image obtained by the oscilloscope for the acoustic signal echo and a GND reference signal from the system.




**Figure 11.** Magnification at the focal length of one image of 8, 9, and 10 acoustic signals.

Figure 12 shows a magnified view at the focal distance of the image obtained from Signal 9 using a conventional probe without attenuation adjustment, set at 2 volts/div. In Figure 12a, it can be observed that the first echo has an amplitude of 1.8 V, while the

second echo measures 400 mV. These low-amplitude echo signals are accompanied by high-frequency noise propagating through the ultrasound system's electronic circuitry. As depicted in Figure 12b, the noise signal was captured using a conventional probe without attenuation adjustment, set at 1 volt/div. This GND signal illustrates how noise propagates within the system, with amplitudes ranging from 80 mV to 1.84 V. Low-amplitude echo signals combined with high-frequency noise are often either suppressed or amplified during signal processing via digital filtering algorithms. This process degrades image quality and simultaneously discards diagnostically relevant information for medical image reconstruction, ultimately reducing the effectiveness of timely medical diagnoses.




(**a**) (**b**)

**Figure 12.** Magnification at the focal distance of the image of (**a**) acoustic signal number nine with the amplitude of the first and second echo and (**b**) noise signal at GND.

## 4. Discussion

The obtained results indicate that the acoustic signals acquired with the oscilloscope through the proposed interface demonstrate the feasibility of measuring, evaluating, and storing the acoustic waveform information from each of the 80 piezoelectric sensors. The relative amount of signal and noise present in a waveform is commonly quantified using the signal-to-noise ratio (SNR). Equation (1) was used, based on the root mean square (RMS) amplitude values of each of the 80 acquired signals. The results are presented in Figure 13, which illustrates the SNR behavior, showing a value of approximately –13 dB. This indicates the presence of noise at a level comparable to or exceeding that of the useful signal power [37]. Such findings suggest that the signals contain a significant level of noise, potentially originating from electronic interference due to power system switching, internal reflections, or limitations of the acquisition system itself. Therefore, to achieve higher-quality analysis or imaging, it would be advisable to apply pre-acquisition filtering and signal processing strategies aimed at increasing the signal-to-noise ratio.

$$SNR = 20 \log \left( \frac{signal}{noise} \right) dB \quad (1)$$

A critical challenge in medical imaging lies in addressing artifacts caused by electromagnetic interference, which degrade ultrasound image quality and diagnostic accuracy. Conventional approaches rely on digital filters and reconstruction algorithms that demand substantial computational resources. However, the simultaneous processing of noise and acoustic signals can suppress diagnostically relevant information or amplify artifacts, potentially introducing false structures in the reconstructed images and compromising diagnostic reliability. Our electronic interface facilitates a deeper understanding of acoustic phenomena in medical systems by enabling the observation of signals in parallel without disrupting the operation of the device, thereby providing the opportunity to analyze and propose effective solutions.

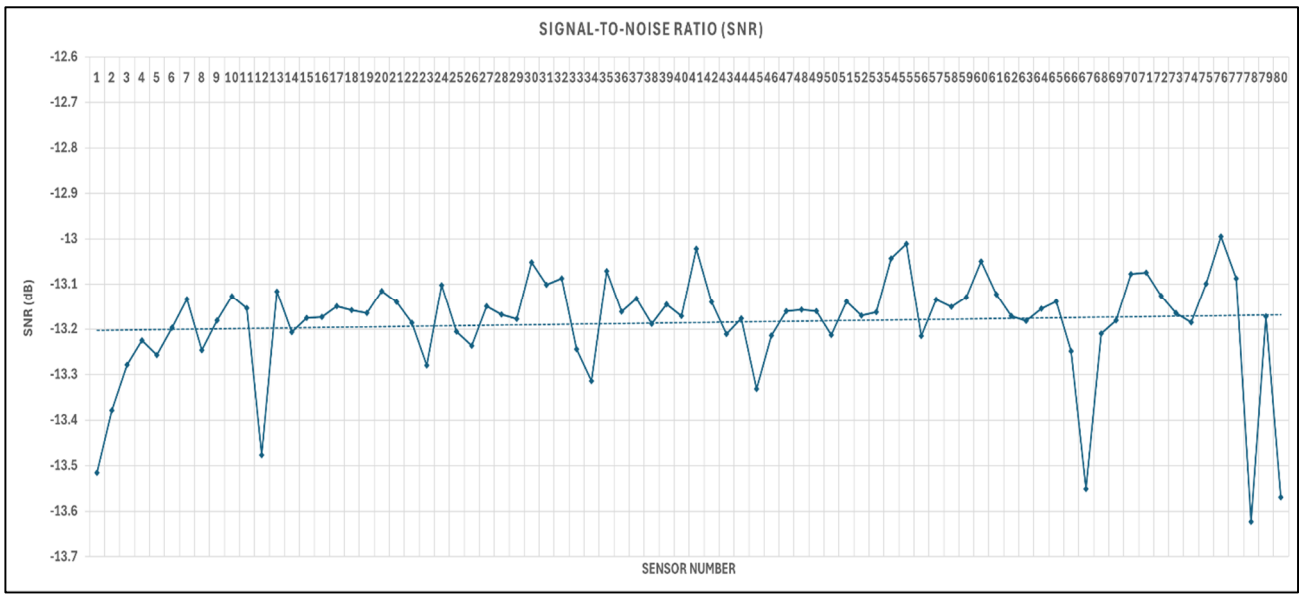



**Figure 13.** Signal-to-noise ratio graph of the 80 sensors in dB.

## 5. Conclusions

This study underscores the critical need for enhancing ultrasound image quality through innovative approaches to optimize medical diagnoses. Ultrasound technology has proven to be remarkably versatile, with applications spanning multiple disciplines, while its advantages over alternative imaging modalities establish it as an indispensable tool in contemporary medicine. Nevertheless, electromagnetic interference and speckle noise persist as major challenges in image reconstruction. Our developed electronic interface facilitates real-time interference analysis and enables the implementation of efficient analog filtering. This approach could decrease dependence on expensive high-performance computing systems while improving medical image quality without loss of diagnostically relevant information. Implementing this technology promises not only more accurate diagnoses, but also advances research in the field, paving the way for innovative solutions in medical imaging. Future work will focus on developing an analog filter for speckle noise elimination. Current digital filtering methods during image reconstruction not only degrade image quality, but also demand excessive computational power. The proposed interface will enable parallel implementation of an analog filtering system, leveraging recent advancements in semiconductor technology that offer high-frequency operation, compact form factors, and cost efficiency. The principal advantage of analog filtering during acoustic signal emission–reception is real-time functional validation. This approach eliminates the need for additional computational processing during image reconstruction, as oscilloscope measurements directly assess filter performance with commercial transducers. This capability allows preliminary evaluation of the analog filter's noise suppression efficacy for high-frequency interference characteristics of medical ultrasound systems prior to full computational system implementation.

**Author Contributions:** Conceptualization, E.E.-R. and M.G.B.-S.; methodology, E.E.-R., M.G.B.-S. and A.G.-L.; software, E.E.-R., J.J.M.-N. and J.A.P.M.; validation, J.A.P.M.; formal analysis, M.G.B.-S., A.G.-L., J.J.M.-N. and F.V.-O.; investigation, E.E.-R. and M.G.B.-S.; resources, E.E.-R., A.G.-L., J.A.P.M., F.V.-O. and E.E.-R.; writing—original draft preparation, E.E.-R., A.G.-L. and M.G.B.-S.; writing—review and editing, E.E.-R. and M.G.B.-S.; supervision, A.G.-L., J.A.P.M., E.E.-R. and F.V.-O.; project administration, E.E.-R. and M.G.B.-S. All authors have read and agreed to the published version of the manuscript.

**Funding:** This research received no external funding.

**Institutional Review Board Statement:** Not applicable.

**Informed Consent Statement:** Not applicable.

**Data Availability Statement:** The original contributions presented in the study are included in the article.

**Conflicts of Interest:** The authors declare no conflicts of interest.

## References

1. Malinowska, N.; Phang, S.; Furniss, D.; Seddon, A.B.; Benson, T.M.; Domagała, Z.; Beres-Pawlik, E. Evolutionary Methods in Clinical Diagnostics. In Proceedings of the 2019 21st International Conference on Transparent Optical Networks (ICTON), Angers, France, 9–13 July 2019; pp. 1–4. [CrossRef]
2. Amini, M.; Liu, P.; Umbaugh, S.E.; Marino, D.J.; Loughin, C.A. Thermographic Image Analysis Method in Detection of Canine Bone Cancer (Osteosarcoma). In Proceedings of the 2012 5th International Congress on Image and Signal Processing, Chongqing, China, 16–18 October 2012; pp. 485–489. [CrossRef]
3. Panayides, A.S.; Amini, A.; Filipovic, N.D.; Sharma, A.; Tsaftaris, S.A.; Young, A.; Foran, D.; Do, N.; Golemati, S.; Kurc, T.; et al. AI in Medical Imaging Informatics: Current Challenges and Future Directions. *IEEE J. Biomed. Health Inform.* **2020**, *24*, 1837–1857. [CrossRef] [PubMed]
4. Ladrova, M.; Martinek, R.; Nedoma, J.; Hanzlikova, P.; Nelson, M.D.; Kahankova, R.; Brablik, J.; Kolarik, J. Monitoring and Synchronization of Cardiac and Respiratory Traces in Magnetic Resonance Imaging: A Review. *IEEE Rev. Biomed. Eng.* **2022**, *15*, 200–221. [CrossRef] [PubMed]
5. Ghosh, K.K.; Padmanabhan, P.; Yang, C.-T.; Ng, D.C.E.; Palanivel, M.; Mishra, S.; Halldin, C.; Gulyás, B. Positron Emission Tomographic Imaging in Drug Discovery. *Drug Discov. Today* **2022**, *27*, 280–291. [CrossRef]
6. Cao, W.; Wu, R.; Cao, G.; He, Z. A Comprehensive Review of Computer-Aided Diagnosis of Pulmonary Nodules Based on Computed Tomography Scans. *IEEE Access* **2020**, *8*, 154007–154023. [CrossRef]
7. Abdulbaqi, H.S.; Mutter, K.N.; Jafri, M.Z.M.; Al-Khafaji, Z.A. Estimation of Brain Tumour Volume Using Expanded Computed Tomography Scan Images. In Proceedings of the 2016 23rd Iranian Conference on Biomedical Engineering and 2016 1st International Iranian Conference on Biomedical Engineering (ICBME), Tehran, Iran, 24–25 November 2016; pp. 117–121. [CrossRef]
8. Verveld, W.; de Wolf, J.R.; Legtenberg, C.G.; Knop, T.; Bosschaart, N. Human Milk Fat Globule Size Distributions: Comparison between Laser Diffraction and 3D Confocal Laser Scanning Microscopy. *Food Res. Int.* **2024**, *198*, 115282. [CrossRef]
9. Neprokin, A.; Broadway, C.; Myllyla, T.; Bykov, A.; Meglinski, I. Photoacoustic Imaging in Biomedicine and Life Sciences. *Life* **2022**, *12*, 588. [CrossRef]
10. Palma-Chavez, J.; Keith, A.; Yash, M.; Jesse, V.; Jokerst, W. Photoacoustic imaging phantoms for assessment of object detectability and boundary buildup artifacts. *Photoacoustics* **2022**, *26*, 100348. [CrossRef]
11. Zhong, Y.; Zhang, S.; Liu, Z.; Zhang, X.; Mo, Z.; Zhang, Y.; Hu, H.; Chen, W.; Qi, L. Unsupervised Fusion of Misaligned PAT and MRI Images via Mutually Reinforcing Cross-Modality Image Generation and Registration. *IEEE Trans. Med. Imaging* **2024**, *43*, 1702–1714. [CrossRef]
12. Baun, J. Advances in Ultrasound Imaging Architecture: The Future Is Now. *J. Diagn. Med. Sonogr.* **2021**, *37*, 312–314. [CrossRef]
13. Tanter, M.; Fink, M. Ultrafast Imaging in Biomedical Ultrasound. *IEEE Trans. Ultrason. Ferroelectr. Freq. Control* **2014**, *61*, 102–119. [CrossRef]
14. Wang, S.; Wang, X.; You, F.; Xiao, H. Review of Ultrasonic Particle Manipulation Techniques: Applications and Research Advances. *Micromachines* **2023**, *14*, 1487. [CrossRef] [PubMed]
15. Xu, Y.; Wang, Y.; Yuan, J.; Cheng, Q.; Wang, X.; Carson, P.L. Medical Breast Ultrasound Image Segmentation by Machine Learning. *Ultrasonics* **2019**, *91*, 1–9. [CrossRef]
16. Jiang, X.; Du, B. Photoacoustic Imaging of Nanoparticle Transport in the Kidneys at High Temporal Resolution. *Angew. Chem.* **2019**, *131*, 6055–6061. [CrossRef]
17. Choi, S.; Young, K. Internal Defect Detection Using Laser-Generated Longitudinal Waves in Ablation Regime. *J. Mech. Sci. Technol.* **2018**, *32*, 4192–4200. [CrossRef]
18. Nyayapathi, N.; Xia, J. Photoacoustic Imaging of Breast Cancer: A Mini Review of System Design and Image Features. *J. Biomed. Opt.* **2019**, *24*, 121911. [CrossRef]
19. Kang, L.; Li, X.; Zhang, Y.; Wong, T.T.W. Deep Learning Enables Ultraviolet Photoacoustic Microscopy Based Histological Imaging with Near Real-Time Virtual Staining. *Photoacoustics* **2022**, *25*, 100308. [CrossRef]

20. Chowdary, J.; Yogarajah, P.; Chaurasia, P.; Guruviah, V. A Multi-Task Learning Framework for Automated Segmentation and Classification of Breast Tumors from Ultrasound Images. *Ultrason. Imaging* **2022**, *44*, 3–12. [CrossRef]
21. Deng, J.; Qu, G.; Ren, S.; Wang, C.; Wang, J.; Zhao, X.; Bai, G. Experimental Study on Acoustic Wave Propagation Characteristics and Main Paths in Loose Coal. *J. China Coal Soc.* **2023**, *48*, 1238–1245.
22. Przybył, K.; Duda, A.; Koszela, K.; Stangierski, J.; Polarczyk, M.; Gierz, Ł. Classification of Dried Strawberry by the Analysis of the Acoustic Sound with Artificial Neural Networks. *Sensors* **2020**, *20*, 499. [CrossRef]
23. Grahama, M.; Huang, J. Simulations and Human Cadaver Head Studies to Identify Optimal Acoustic Receiver Locations for Minimally Invasive Photoacoustic-Guided Neurosurgery. *Photoacoustics* **2020**, *19*, 100183. [CrossRef]
24. Huang, Y.; Das, P.K.; Bhethanabotla, V.R. Surface Acoustic Waves in Biosensing Applications. *Sens. Actuators Rep.* **2021**, *3*, 100041. [CrossRef]
25. Mandal, D.; Banerjee, S. Surface Acoustic Wave (SAW) Sensors: Physics, Materials, and Applications. *Sensors* **2022**, *22*, 820. [CrossRef] [PubMed]
26. Gallo, M.; Ferrara, L.; Naviglio, D. Application of Ultrasound in Food Science and Technology: A Perspective. *Foods* **2018**, *7*, 164. [CrossRef] [PubMed]
27. Hakakzadeh, S.; Mozaffarzadeh, M. Multi-Angle Data Acquisition to Compensate Transducer Finite Size in Photoacoustic Tomography. *Photoacoustics* **2022**, *27*, 100373. [CrossRef]
28. Steinberg, I.; Schneider, M. Superiorized Photo-Acoustic Non-Negative Reconstruction (SPANNER) for Clinical Photoacoustic Imaging. *IEEE Trans. Med. Imaging* **2021**, *40*, 1888–1897. [CrossRef]
29. Yang, G.; Amidi, E. Photoacoustic Tomography Reconstruction Using Lag-Based Delay Multiply and Sum with a Coherence Factor Improves In Vivo Ovarian Cancer Diagnosis. *Biomed. Opt. Express* **2021**, *12*, 2250–2263. [CrossRef]
30. Ruiz, M.; Gutiérrez, G.; Polo, L.; Cortalezzi, F. Image Reconstruction Algorithm for Laser-Induced Ultrasonic Imaging: The Single Sensor Scanning Synthetic Aperture Focusing Technique. *J. Acoust. Soc. Am.* **2023**, *153*, 560–572. [CrossRef]
31. Garcia, D. SIMUS: An Open-Source Simulator for Medical Ultrasound Imaging. Part I: Theory & Examples. *Comput. Methods Programs Biomed.* **2022**, *218*, 106726. [CrossRef]
32. Quien, M.M.; Saric, M. Ultrasound Imaging Artifacts: How to Recognize Them and How to Avoid Them. *Echocardiography* **2018**, *35*, 1388–1401. [CrossRef]
33. Claudon, M.; Bergès, O. Artifacts in Ultrasound. In *Echography of the Eye and Orbit*; Bergès, O., Ed.; Springer: Cham, Germany, 2024. [CrossRef]
34. Hakakzadeh, S.; Amjadian, M.; Zhang, Y.; Mostafavi, S.; Kavehvash, Z.; Wang, L. Signal Restoration Algorithm for Photoacoustic Imaging Systems. *Biomed. Opt. Express* **2023**, *14*, 651–666. [CrossRef]
35. Kremkau, F.W.; Taylor, K.J. Artifacts in Ultrasound Imaging. *J. Ultrasound Med.* **1986**, *5*, 227–237. [CrossRef] [PubMed]
36. Huber, M.T.; Flint, K.M.; McNally, P.J.; Ellestad, S.C.; Trahey, G.E. Human Observer Sensitivity to Temporal Noise During B-Mode Ultrasound Scanning: Characterization and Imaging Implications. *Ultrason. Imaging* **2024**, *46*, 151–163. [CrossRef] [PubMed]
37. Gokhan, G.; Nasire, U.; Aytac, D.; Aytac, E. Comparison of Noise Reduction Methods in Photoacoustic Microscopy. *Comput. Biol. Med.* **2019**, *109*, 333–341. [CrossRef]
38. Choi, H.; Jeong, J. Despeckling Algorithm for Removing Speckle Noise from Ultrasound Images. *Symmetry* **2020**, *12*, 938. [CrossRef]
39. Duarte, A.; Castro, M.A.B.; Becerra, E.; Delgado-Trejos, E. Speckle Noise Reduction in Ultrasound Images for Improving the Metrological Evaluation of Biomedical Applications: An Overview. *IEEE Access* **2020**, *8*, 15983–15999. [CrossRef]
40. Rodríguez, N.A.; Cruz, V.; Gómez, A.; Hernández-Alvarado, R.; Nava-Balanzar, L.; Salgado-Jiménez, T.; Soto-Cajiga, J.A. Improvement of Ultrasonic Pulse Generator for Automatic Pipeline Inspection. *Sensors* **2018**, *18*, 2950. [CrossRef]
41. Bushberg, J.T.; Seibert, J.A.; Leidholdt, E.M.; Boone, J.M. *The Essential Physics of Medical Imaging*, 3rd ed.; Lippincott Williams and Wilkins: Philadelphia, PA, USA, 2011.
42. Mahesh, M. The Essential Physics of Medical Imaging, Third Edition. *Med. Phys.* **2013**, *40*, 077301. [CrossRef]
43. Balcells, J. *Interferencias Electromagnéticas en Sistemas Electrónicos*; Marcombo: Barcelona, Spain, 1991.
44. Veraguas, J.P.L. *Compatibilidad Electromagnética y Seguridad Funcional en Sistemas Electrónicos*; Marcombo: Barcelona, Spain, 2010.
45. Banco de México. Moneda de 50 Centavos de la Familia D, Circulación. Available online: https://www.banxico.org.mx (accessed on 2 May 2025).


**Disclaimer/Publisher's Note:** The statements, opinions and data contained in all publications are solely those of the individual author(s) and contributor(s) and not of MDPI and/or the editor(s). MDPI and/or the editor(s) disclaim responsibility for any injury to people or property resulting from any ideas, methods, instructions or products referred to in the content.